Title
Geomagnetic polar minima do not arise from steady meridional circulation

Journal
Proceedings of the National Academy of Sciences of the United States of America, 115(44)

ISSN
0027-8424

Authors
Cao, Hao
Yadav, Rakesh K
Aurnou, Jonathan M

Publication Date
2018-10-30

DOI
10.1073/pnas.1717454115

Peer reviewed

Geomagnetic polar minima do not arise from steady meridional circulation

Hao Cao[a,b,1], Rakesh K. Yadav[a], and Jonathan M. Aurnou[c]

[a]Department of Earth and Planetary Sciences, Harvard University, Cambridge, MA 02138; [b]Division of Geological and Planetary Sciences, California Institute of Technology, Pasadena, CA 91125; and [c]Department of Earth, Planetary, and Space Sciences, University of California, Los Angeles, CA 90095

Edited by Peter L. Olson, Johns Hopkins University, Baltimore, MD, and approved September 18, 2018 (received for review October 4, 2017)

Observations of the Earth's magnetic field have revealed locally pronounced field minima near each pole at the core–mantle boundary (CMB). The existence of the polar magnetic minima has long been attributed to the supposed large-scale overturning circulation of molten metal in the outer core: Fluid upwells within the inner core tangent cylinder toward the poles and then diverges toward lower latitudes when it reaches the CMB, where Coriolis effects sweep the fluid into anticyclonic vortical flows. The diverging near-surface meridional circulation is believed to advectively draw magnetic flux away from the poles, resulting in the low intensity or even reversed polar magnetic fields. However, the interconnections between polar magnetic minima and meridional circulations have not to date been ascertained quantitatively. Here, we quantify the magnetic effects of steady, axisymmetric meridional circulation via numerically solving the axisymmetric magnetohydrodynamic equations for Earth's outer core under the magnetostrophic approximation. Extrapolated to core conditions, our results show that the change in polar magnetic field resulting from steady, large-scale meridional circulations in Earth's outer core is less than 3% of the background field, significantly smaller than the ∼100% polar magnetic minima observed at the CMB. This suggests that the geomagnetic polar minima cannot be produced solely by axisymmetric, steady meridional circulations and must depend upon additional tangent cylinder dynamics, likely including nonaxisymmetric, time-varying processes.

geodynamo | polar magnetic minima | polar vortex | gyroscopic pumping | flow magnetic field interactions

In an era of in situ exploration of planetary bodies in the solar system and remote exploration of planetary bodies outside the solar system, the intrinsic magnetic field of the Earth (1, 2), the best documented of all planetary magnetic fields (3, 4), serves as a key test of our understanding of the planetary dynamo mechanism. A few distinct features stand out in the present-day geomagnetic field when downward extrapolated to the core–mantle boundary (CMB) (Fig. 1) (5). Here we will focus on the region within the so-called tangent cylinder (TC), which is the imaginary cylinder co-axial with the spin axis and tangent to the inner core's equator (Fig. 1*C*). Within the TC, the radial magnetic field on the CMB features weak and even reversed magnetic flux patches in both hemispheres, commonly referred to as polar magnetic minima (6). The amplitude of the relative axisymmetric polar magnetic minima is defined as

$$\frac{|dB_r|}{|B_r^{max}|} = \frac{|B_r^{pole} - B_r^{max}|}{|B_r^{max}|}, \qquad [1]$$

where B_r^{max} (B_r^{pole}) is the maximum (polar) value of the azimuthally averaged, radial magnetic field on the CMB. The value of $|dB_r|/|B_r^{max}|$ is ∼100% for the northern hemisphere and ∼60% for the southern hemisphere (Fig. 1*B*).

By tracking the time evolution of the polar magnetic minima and attributing the changes in the magnetic field to steady-state axisymmetric advection by core flows, Olson and Aurnou (12) inferred the existence of an axisymmetric, anticyclonic polar vortex inside the TC near the surface of the outer core with characteristic azimuthal velocity $u_\phi \sim 0.1$ mm/s. A similar axisymmetric CMB flow field was found via inversion of the high-resolution Ørsted satellite magnetic field data (13) and in subsequent studies using different assumptions and datasets (14, 15). The magnetic Reynolds number associated with the inferred ~ 0.1 mm/s polar vortex, defined as $Rm = u_\phi R_C/\eta$, is ∼500, taking the core radius $R_C = 3485$ km for length scale and $\eta \sim 0.8$ m^2/s as the magnetic diffusivity (16, 17). The possibility of such a polar vortex extending axially throughout the TC, and its connection to the seismically inferred inner core superrotation, has been extensively investigated (18–23). TC-filling polar vortices have also been found in a number of geodynamo models (7, 11, 20, 24). Thus, an axisymmetric polar vortex is presently the canonical flow believed to exist within the TC (e.g., figure 1 in ref. 11 and Fig. 1*C*).

Recent high-resolution geomagnetic field inversions have suggested the possibility of an alternative scenario in which an accelerating nonaxisymmetric jet exists along the TC rim (25). Additionally, seismic observations suggest a shuffling rotation of the Earth's inner core, switching between superrotation and subrotation on a decadal time scale (22), rather than the constant superrotation that would better support the existence of quasi-steady, axisymmetric polar vortices. These studies call into question the leading interpretation of the polar magnetic minima, in which meridional circulation associated with the inferred polar vortices advects magnetic flux away from the poles below the

Significance

The geomagnetic field provides one of the best diagnostics of Earth's core dynamics. In the polar regions of the core–mantle boundary (CMB), the geomagnetic field features weak and even reserved magnetic fluxes that have been referred to as polar magnetic minima. The origin of the geomagnetic polar minima has been commonly attributed to divergent advection of magnetic fluxes by meridional circulation associated with anticyclonic polar vortices. In this study, we performed a quantitative evaluation of this canonical picture. Our analysis showed that steady meridional circulation associated with observed anticyclonic polar vortices are not capable of creating the observed geomagnetic polar minima. We propose three alternative possibilities for the origin of the geomagnetic polar minima.

Author contributions: H.C. and J.M.A. designed research; H.C. and R.K.Y. performed research; H.C. and R.K.Y. analyzed data; and H.C. and J.M.A. wrote the paper.

The authors declare no conflict of interest.

This article is a PNAS Direct Submission.

Data deposition: The snapshots reported in this paper are available in Movie S1 and on Figshare, https://doi.org/10.6084/m9.figshare.7152665.

[1]To whom correspondence should be addressed. Email: haocao@fas.harvard.edu.

This article contains supporting information online at www.pnas.org/lookup/suppl/doi:10.1073/pnas.1717454115/-/DCSupplemental.

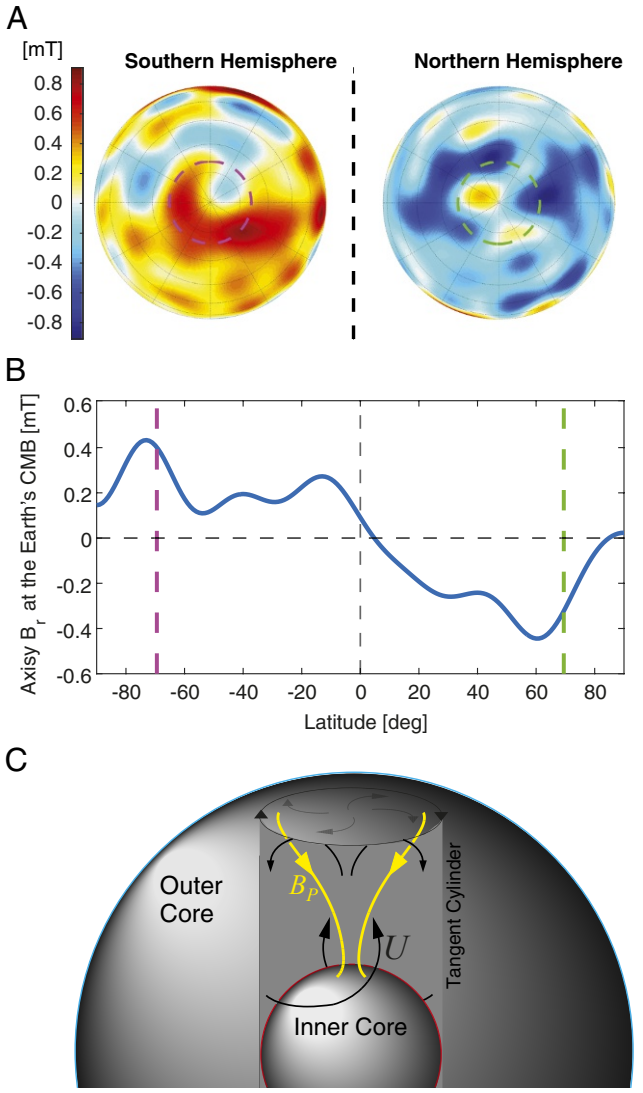

Fig. 1. Current epoch geomagnetic field at the Earth's CMB (5) and the canonical picture of the origin of polar magnetic minima (7–11). (*A*) The radial component of the geomagnetic field at the CMB (5). The southern hemisphere is shown in *Left*, while the northern hemisphere is shown in *Right*. It can be seen that the region poleward of the TC (pink and green dashed circles) features weak and reserved magnetic flux in both hemispheres. (*B*) The axisymmetric radial magnetic field at the CMB. The relative amplitude of the axisymmetric polar magnetic minima, $|dB_r|/|B_r^{max}|$, is $\sim 100\%$ ($\sim 60\%$) in the northern (southern) hemisphere. (*C*) The leading explanation for the origin of the polar magnetic minima: Meridional circulation associated with the inferred TC polar vortex advects magnetic flux away from the poles. (*C*) Poloidal magnetic field lines are shown as yellow lines, and velocities are marked by black lines.

CMB (7–11, 26). Furthermore, the essential hypotheses underlying this idea remain untested since neither (i) the amplitude of the meridional circulation associated with the polar vortices nor (ii) the amplitude of the polar magnetic minima associated with the meridional circulation have been quantified. To address this deficit, we determine here under what conditions the meridional circulations associated with steady, axisymmetric polar vortices are capable of generating polar magnetic minima of comparable strength to those observed. Steady, magnetostrophically balanced core flow, which can be convection-driven (e.g., thermal plume) or Lorentz-force–driven, is the focus of this study.

Ekman Pumping and Gyroscopic Pumping

Before delving into the modeling efforts, we first develop scaling predictions for the strength of polar meridional circulations. In rapidly rotating fluid systems, net transport occurs in the direction perpendicular to both the net body/surface force $F\hat{f}$ and the spin-axis $\hat{z}$, as dictated by the local force balance between $F\hat{f}$ and the Coriolis forces (e.g., refs. 27–29):

$$2\rho_0\Omega\hat{z}\times\mathbf{u}=F\hat{f}, \qquad [2]$$

where ρ_0 is the fluid density, Ω is the background rotation rate, and $\mathbf{u}$ is the fluid transport velocity. For example, a negative zonal force (zonal corresponds to azimuthal) would require flows away from the spin axis in the positive cylindrical radial direction $(+\hat{s})$, while a positive zonal force would require flows toward the spin axis $(-\hat{s})$. Mass conservation necessitates the existence of flows in the vertical direction $(\pm\hat{z})$, giving rise to a global meridional circulation (*SI Appendix*, Figs. S2 and S5).

In the hydrodynamic context of atmospheric and oceanic dynamics, this phenomenon is referred to as Ekman pumping (e.g., refs. 27–29). In systems with stress-free mechanical boundary conditions, Ekman pumping effects generate a net meridional transport u_{MC} that scales linearly with the Ekman number, E, the ratio of viscous and Coriolis forces. In contrast, when the boundary conditions are no-slip, boundary layer processes alter the pumping efficiency such that $u_{MC}\sim E^{1/2}$.

The generalization of Ekman pumping to magnetohydrodynamic (MHD) systems is called gyroscopic pumping and has been extensively investigated in the context of stellar interior dynamics (e.g., refs. 30 and 31). In gyroscopic pumping, the force that pumps the fluid can be any body force, including Lorentz forces. Here we emphasize that gyroscopic pumping describes a balanced state, rather than specifying the causality between the force and the flows, which is an intricate question for a fully dynamical system (see *SI Appendix* for more discussion). The cylindrical radial velocity u_s associated with the Lorentz force in the zonal direction $F_{L,\phi}$ is

$$u_s=\frac{F_{L,\phi}}{2\rho_0\Omega}. \qquad [3]$$

Under axisymmetry, the Lorentz force becomes

$$F_{L,\phi}^{axi}=\frac{\mathbf{B}_{r,\theta}^{axi}\times(\nabla\times\mathbf{B}_{\phi}^{axi})}{\mu_0}, \qquad [4]$$

where μ_0 is the magnetic permeability and $\mathbf{B}_{r,\theta}^{axi}$ and $\mathbf{B}_{\phi}^{axi}$ are the axisymmetric meridional (or poloidal) magnetic field and the axisymmetric zonal (or toroidal) magnetic field, respectively. From here onwards, we consider only axisymmetric quantities and drop all axi superscripts. The efficiency of meridional circulation to advect magnetic flux can be assessed via the magnetic Reynolds number

$$Rm_{MC}=\frac{u_s D}{\eta}\sim\frac{1}{2}\sqrt{\Lambda(B_{r,\theta})}\sqrt{\Lambda(B_{\phi})}, \qquad [5]$$

where D is the typical length scale and Λ is the Elsasser number

$$\Lambda=\frac{B^2}{\mu_0\eta\rho_0\Omega} \qquad [6]$$

that estimates the ratio of Lorentz and Coriolis forces and is of order unity on Earth's CMB (4). Recent low-viscosity numerical dynamo simulations (24, 32, 33) also find Elsasser numbers associated with the internal magnetic field to be between 0.4 and 32, in basic agreement with the $\Lambda\sim 1$ predictions of asymptotic

theory (34). Thus, the magnetic Reynolds number associated with steady-state meridional circulation is likely to be of order unity in Earth's core. This $Rm_{MC} \sim \Lambda \sim 1$ value is likely too low to generate the $\sim$100% deviations in the polar geomagnetic field, suggesting that additional processes are required to explain the observed polar geomagnetic minima.

Numerical Method

Our axisymmetric model uses a pseudospectral method to solve for Boussinesq flows ($\nabla \cdot \mathbf{U} = 0$, $\nabla \cdot \mathbf{B} = 0$, $\partial/\partial\phi = 0$) under the magnetostrophic approximation (2, 35) in which the inertia terms in the momentum equation, including the time-dependent term and the advection term, are neglected. The nondimensional momentum equation is then

$$2\hat{z} \times \mathbf{U} + \nabla\Pi = (\nabla \times \mathbf{B}) \times \mathbf{B} + \mathcal{A}_{\mathcal{TW}}\, T\vec{r} + E\nabla^2\mathbf{U}, \qquad [7]$$

and the nondimensional electromagnetic induction equation is

$$\frac{\partial \mathbf{B}}{\partial t} = \nabla \times (\mathbf{U} \times \mathbf{B}) + \nabla^2\mathbf{B}, \qquad [8]$$

where Π is the nonhydrostatic pressure, T is the temperature perturbation, $\mathbf{U}$ is the velocity, $\mathbf{B}$ is the magnetic field, ϕ is the azimuthal angle, $\hat{z}$ is the unit vector parallel to the spin axis, and $\vec{r}$ is the spherical radius vector measured from the origin of the coordinate system. In our nondimensionalization, the length scale is the core radius R_C, the time scale is the magnetic diffusion time R_C^2/η, the magnetic field scale is $\sqrt{\mu_0\eta\rho_0\Omega}$ (i.e., $\Lambda^{1/2}$ units), the temperature scale is $\Omega\eta/\alpha g_0 R_C$ where α is the thermal expansivity and g_0 is the gravitational acceleration at the CMB, $\mathcal{A}_{\mathcal{TW}}$ is a coefficient used to vary the strength of the thermal forcing, and the Ekman number is defined as $E = \nu/\Omega R_C^2$ in which ν is the kinematic viscosity.

The flows in our axisymmetric magnetostrophic models are driven by the latitudinal gradient of the axisymmetric temperature field, $\partial T(r,\theta)/\partial\theta$. The temperature pattern, $T(r,\theta)$, is taken from a 3D dynamo calculation described in *SI Appendix*. The amplitude of the thermal forcing is set by the value of $\mathcal{A}_{\mathcal{TW}}$. The strength of the viscous forces is controlled by the value of the Ekman number E. The magnetic field is composed of two components, the induced field and an imposed, current-free poloidal field $\mathbf{B}_{imp}$. The geometry and amplitude of $\mathbf{B}_{imp}$ is varied via different combinations of associated Legendre polynomials. The root-mean-squared amplitude of the imposed field is reported via the Elsasser number $\Lambda_{imp} = B^2_{imp,rms}$. Details of our axisymmetric magnetostrophic numerical implementation are given in *SI Appendix*.

Furthermore, we augment the axisymmetric magnetostrophic models with fully three-dimensional (3D) global numerical geodynamo simulations with Ekman number varying from 10^{-4} to 10^{-6} (32). Details of the 3D global geodynamo simulations are given in *SI Appendix* and in ref. 32.

Results

Two sets of axisymmetric, magnetostrophic numerical experiments are carried out. In the first set of so-called "kinematic" experiments, Lorentz force is not taken into account in the momentum (Eq. **7**). The momentum equation is purely hydrodynamic. For cases with stress-free and no-slip mechanical boundary conditions, we respectively predict E and $E^{1/2}$ for the amplitude scaling of meridional circulation as well as for the amplitude of the relative polar magnetic minima, $|dB_r|/|B_r^{max}|$.

In the second set of "dynamic" experiments, the Lorentz forces are self-consistently accounted for in solving Eq. **7**. In the dynamic experiments, we observe the interplay among three classical processes that occur in rapidly rotating MHD: dynamo ω-effects (2), Taylor's constraint (36), and gyroscopic pumping (30, 31). Misalignment between zonal flows and poloidal magnetic field induces electric currents (i.e., the ω-effect) and zonal Lorentz forces, the local zonal Lorentz force requires meridional circulation (gyroscopic pumping), and the nonzero z-integration of the Lorentz force can drive strong z-invariant zonal flows (Taylor's constraint). The nonlinear interplay among these three effects drives the system toward a state in which the zonal flow and the poloidal magnetic field becomes better aligned. Although we predict that $u_s \propto \sqrt{\Lambda(B_{r,\theta})\Lambda(B_\phi)}$, the multiple nonlinear feedbacks necessitate a forward modeling approach to determine the scaling behaviors of u_s and $|dB_r|/|B_r^{max}|$ in the fully dynamic MHD system.

Examples of zonal flows, meridional circulations, and magnetic fields from our kinematic and dynamic calculations are presented in *SI Appendix*, Fig. S2. These no-slip cases are carried out with $E = 3 \times 10^{-6}$, $\mathcal{A}_{\mathcal{TW}} = 600$, and a uniform axial-imposed magnetic field of amplitude $\Lambda_{imp} = 1$. Strong zonal flows have been generated within the TC with $Rm(u_\phi) \sim 100$ in the kinematic case and $Rm(u_\phi) \sim 250$ in the dynamic case. Anticyclonic (polar) vortices exist below the CMB in both cases, however a cyclonic vortex exists above the inner core boundary (ICB) only in the kinematic case. In the dynamic case, the violation of the Taylor's constraint (36) generates a strong z-invariant zonal flow (37, 38), which swamps the cyclonic vortical flow near the ICB (*SI Appendix*, Figs. S2 and S3). Ekman pumping induces a meridional circulation with a peak amplitude of order $Rm(u_s) \sim 0.02$ in the kinematic case. In contrast, gyroscopic pumping induces a meridional circulation with a peak amplitude of $Rm(u_s) \sim 10$ in the dynamic case, exceeding the kinematic response by nearly 500 times. The stronger meridional circulation in the dynamic case generates far stronger polar magnetic minima relative to the kinematic case (Fig. 2 and *SI Appendix*, Fig. S2). The

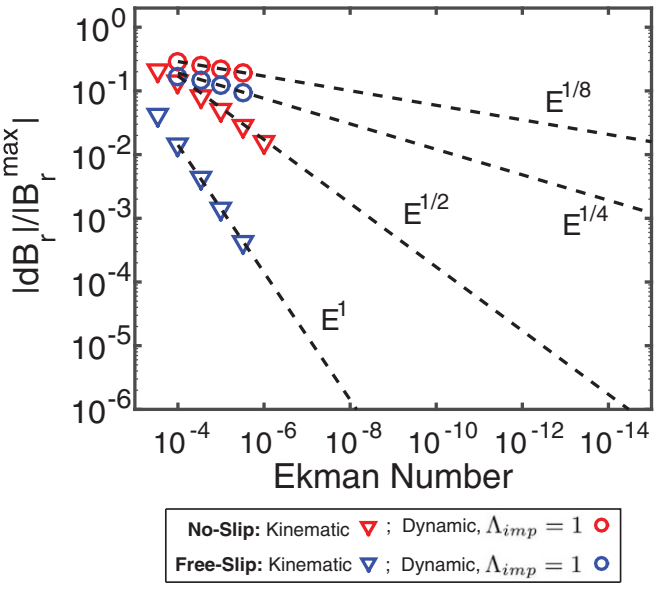

Fig. 2. Relative amplitude of polar magnetic minima, $|dB_r|/|B_r^{max}|$, as a function of the Ekman number from kinematic and dynamic magnetostrophic calculations at $\mathcal{A}_{\mathcal{TW}} = 300$ and an imposed, axial $\Lambda = 1$ magnetic field. In the kinematic surveys, $|dB_r|/|B_r^{max}|$ follow the predicted $E^{1/2}$ scaling with no-slip boundary conditions and the E^1 scaling with free-slip boundary conditions. In the dynamic surveys with self-consistently calculated Lorentz force, the polar magnetic minima are enhanced due to gyroscopic pumping and follow a $\sim E^{1/4}$ scaling in the free-slip cases and a $\sim E^{1/8}$ scaling in the no-slip cases, which result from the nonlinear feedbacks that exist between the zonal flows, magnetic fields, and Lorentz forces.

(cylindrical) radial flow in our dynamic magnetostrophic models is not limited to the boundary layers at the top and bottom of the outer core but fills the entire outer core (*SI Appendix*, Figs. S2*C* and S5*C*).

Fig. 2 shows the amplitude of the relative polar magnetic minima as a function of the Ekman number from kinematic and dynamic calculations at $\mathcal{A}_{\mathcal{TW}} = 300$ and Λ_{imp}(uniform B_z) $= 1$. The meridional circulation in the kinematic surveys comes solely from the viscous Ekman pumping. It can be seen from Fig. 2 that the relative amplitude of polar magnetic minima in the kinematic surveys follows the classical $E^{1/2}$ scaling in the no-slip cases and the E^1 scaling in the free-slip cases (38). In the no-slip kinematic cases,

$$\frac{|dB_r|}{|B_r^{max}|} = 0.32 Rm(u_\phi) E^{1/2}, \quad [9]$$

while in the free-slip kinematic cases,

$$\frac{|dB_r|}{|B_r^{max}|} = 2.82 Rm(u_\phi) E^{1}, \quad [10]$$

where the value of the azimuthal magnetic Reynolds number $Rm(u_\phi)$ is controlled by the thermal forcing (*SI Appendix*, Fig. S1). Given that $Rm(u_\phi)$ of the inferred anticyclonic polar vortex at the Earth's outer core is ~ 500 (12, 16, 17) and E of the Earth's core is $\sim 1 \times 10^{-15}$, our kinematic survey predicts the relative polar magnetic minima associated with Ekman pumping to be on the order of 5×10^{-6} for the Earth's core under no-slip boundary conditions. This is many orders of magnitude smaller than the observed $\sim 100\%$ polar magnetic minima at the Earth's CMB. In contrast, for a modest Ekman number commonly adopted in 3D geodynamo simulations such as $E = 3 \times 10^{-5}$, our kinematic survey predicts $|dB_r|/|B_r^{max}|$ as large as 88% for $Rm(u_\phi) = 500$ with no-slip boundary conditions and $\sim 4\%$ with free-slip boundary conditions. The strong $|dB_r|/|B_r^{max}|$ signatures of viscous Ekman pumping likely then influence the global field strengths and the large-scale field morphologies in moderate Ekman number dynamo studies with no-slip boundary conditions (e.g., refs. 26, 39, and 40). We will return to this point later when examining our own 3D numerical dynamo simulations (32).

In the dynamic surveys with $\mathcal{A}_{\mathcal{TW}} = 300$, $|dB_r|/|B_r^{max}|$ follows a $E^{1/8}$ scaling in the no-slip cases and a $E^{1/4}$ scaling in the free-slip cases (Fig. 2). In the no-slip dynamic cases with $\mathcal{A}_{\mathcal{TW}} = 300$,

$$\frac{|dB_r|}{|B_r^{max}|} = 1.06 E^{1/8}, \quad [11]$$

while in the free-slip dynamic cases with $\mathcal{A}_{\mathcal{TW}} = 300$,

$$\frac{|dB_r|}{|B_r^{max}|} = 2.2 E^{1/4}. \quad [12]$$

We have varied $\mathcal{A}_{\mathcal{TW}}$ from 300 to 6,000 and observed similar, but not constant, scalings with the Ekman number in our dynamic surveys (*SI Appendix*, Fig. S4). The inclusion of Lorentz forces drives much stronger polar vortical flows in the dynamic calculations, with strong z-invariant component of the zonal flows (36–38). For example, at $E = 3 \times 10^{-6}$ and $\mathcal{A}_{\mathcal{TW}} = 600$, the amplitude of the z-invariant zonal flow inside the TC exceeds that of the z-varying zonal flow (thermal wind) in both the free-slip case and the no-slip case (*SI Appendix*, Figs. S2 and S3). These calculations point to the possibility that a significant fraction of the observed anticyclonic polar vortices at the Earth's outer core could be z-invariant, which would differ from the results of most 3D numerical geodynamo simulations (24, 26, 41).

Next, we extrapolate our scaling results to Earth's core. We use the dynamic scalings derived from both no-slip cases and free-slip cases. The amplitude of the z-invariant zonal flows scales as $E^{-1/2} \int_z F_{Lorentz,\phi} dz$ with no-slip boundary conditions and scales as $E^{-1} \int_z F_{Lorentz,\phi} dz$ with free-slip boundary conditions (37, 38). Thus, free-slip cases at $E = 3 \times 10^{-8}$ should serve as a proxy for no-slip cases at $E = 10^{-15}$. The amplitude of the polar vortex in the free-slip dynamic calculations at $E = 3 \times 10^{-6}$, $\mathcal{A}_{\mathcal{TW}} = 300$ already exceeds the inferred polar vortex amplitude in Earth's core ($Rm(u_\phi) \simeq 500$). Within the framework of our dynamic magnetostrophic models, we regard $\mathcal{A}_{\mathcal{TW}} = 300$ as an upper bound of thermal forcing for $Rm(u_\phi) \simeq 500$. The predicted polar magnetic minima is $\sim 3\%$ when we extrapolate the $E^{1/4}$ dynamic free-slip scaling to $E = 3 \times 10^{-8}$ and $\sim 1.4\%$ when we extrapolate the $E^{1/8}$ dynamic no-slip scaling to $E = 10^{-15}$. However, even the 3% estimate is more than an order of magnitude smaller than the observed 60–100% polar magnetic minima at the Earth's CMB.

The zonal Lorentz force and the cylindrical radial velocity (u_s) in the dynamic free-slip calculations with $\mathcal{A}_{\mathcal{TW}} = 300$, $E = 3 \times 10^{-6}$, Λ_{imp}(uniform B_z) $= 1$ are shown in *SI Appendix*, Fig. S5. The amplitude of the meridional circulation, as measured by $Rm(u_s)$, is indeed on the order of unity as predicted by our simple order of magnitude analysis of the Lorentz-force–driven gyroscopic pumping (Eq. **5**). Moreover, *SI Appendix*, Fig. S5*C* shows the gradual decrease in the amplitude of the meridional circulation in the dynamic calculations as the Ekman number decreases. This decrease in the amplitude of the meridional circulation results from the decrease of zonal Lorentz force and is responsible for the corresponding scaling of $|dB_r|/|B_r^{max}|$ with the Ekman number in the dynamic calculations.

The geometry (*SI Appendix*, Fig. S1) and amplitude of the imposed poloidal magnetic fields have been varied in our numerical experiments. These calculations show that the geometry of the imposed axisymmetric magnetic field does not fundamentally alter the amplitude and scaling of the resulted polar magnetic minima (*SI Appendix*, Fig. S6). When the amplitude of the imposed field is varied, $|dB_r|/|B_r^{max}|$ reaches the maximum when the Elsasser number of the imposed poloidal magnetic field is in the range of 1 to 10 in the dynamic calculations, as shown in *SI Appendix*, Fig. S7. Further, the same $\sim E^{1/4}$ scaling at $\mathcal{A}_{\mathcal{TW}} = 300$ is found for $|dB_r|/|B_r^{max}|$ in stress-free dynamic calculations at $\Lambda_{imp} = 10$. These results imply then that

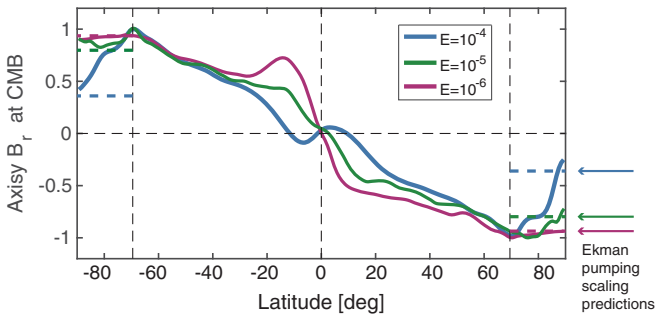

Fig. 3. Axisymmetric radial magnetic field at the CMB, scaled to the peak B_r, from 3D global numerical dynamo simulations with $Rm(u_\phi, TC) \sim 200$ at three different Ekman numbers: 10^{-4}, 10^{-5}, and 10^{-6}. For all three Ekman numbers, the polar magnetic minima in the 3D runs are in good agreement with that associated with Ekman pumping predicted by our scaling [**9**], $0.32 Rm(u_\phi) E^{1/2}$, the values of which are shown via the dashed horizontal lines and arrows of the respective colors. For all three Ekman numbers, a random snapshot is chosen that is representative of the entire run (see *SI Appendix*, Movie S1; also available at https://doi.org/10.6084/m9.figshare.7152665).

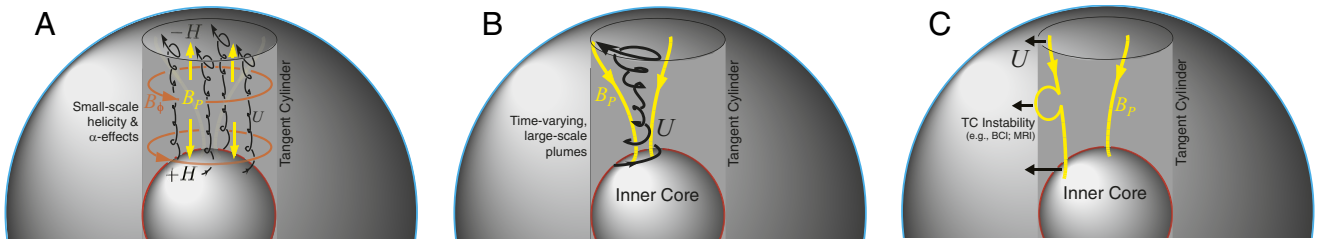

Fig. 4. Sketch of alternative scenarios for the origin of polar magnetic minima. (*A*) Small-scale dynamo action within the TC, which could create polar magnetic minima by actively generating a radial magnetic field of opposite sign to the background magnetic field in the vicinity of the CMB. (*B*) Large-scale nonaxisymmetric and/or time-varying polar upwellings that could carry reversed flux upwards toward the poles. (*C*) A large-scale instability of the TC, which could generate large-scale magnetic field structures near the edge of the TC.

the amplitude and scaling of $|dB_r|/|B_r^{max}|$ are robust for the estimated range of magnetic field strength, $10^{-1} \lesssim \Lambda \lesssim 10$, in the Earth's outer core.

To augment our highly reduced magnetostrophic models, we have analyzed the polar magnetic field properties from global 3D numerical dynamo simulations in which the Ekman number varies from 10^{-4} to 10^{-6} (32). In particular, we selected various E cases from ref. 32 in which $Rm(u_\phi, TC) \sim 200$ and the convective flow stays between 10 to 15 times supercritical. It can be seen from Fig. 3 that the resulted polar magnetic minima in a typical snapshot of the 3D global dynamo runs become less and less prominent as the Ekman number decreases from 10^{-4} to 10^{-6}. For all three Ekman numbers, the polar magnetic minima in the 3D runs are in good agreement with that associated with Ekman pumping predicted by our scaling [**9**], $0.32Rm(u_\phi)E^{1/2}$, the values of which are shown via the dashed horizontal lines and arrows of the respective colors. For all three cases, a random snapshot is chosen. These random snapshots are representative of the entire run, as can be seen from *SI Appendix*, Movie S1 (also available at https://doi.org/10.6084/m9.figshare.7152665).

Summary and Discussion

Our inertia-free, axisymmetric numerical simulations show that the meridional circulation associated with the canonical TC polar vortex flow (Fig. 1*C*) is in basic agreement with the order-of-magnitude estimate of the Lorentz-force–driven gyroscopic pumping [**5**]. This meridional circulation indeed advects magnetic flux away from the polar regions. However, extrapolating our results to Earth's core conditions, we find that the magnitude of the polar magnetic minima would be more than an order of magnitude smaller than those observed (Fig. 2). The physical picture and scaling derived from our inertia-free, axisymmetric numerical simulations are in good agreement with low Ekman number 3D global geodynamo simulations as shown in Fig. 3. Our results suggest that physical processes beyond quasi-steady meridional circulation are necessary to explain the observed $\sim$100% geomagnetic polar minima.

Here we propose three possible alternative mechanisms for the origin of the geomagnetic polar minima, as summarized in Fig. 4. In the first scenario, we assume, in addition to a large-scale polar vortex, that strong, smaller scale convective turbulence fills the TC volume (e.g., ref. 42). Assuming the flow is predominantly driven by a vertical buoyancy flux emanating from the ICB, vortex stretching will act to generate positive axially helical flow, H, in the vicinity of the ICB and negative helicity flow near the CMB (e.g., refs. 43 and 44). The helical flow will give rise to TC-localized α-effects (2) that will induce positive (negative) B_r near the CMB in the presence of positive (negative) B_ϕ generated by the large-scale polar vortex. In both hemispheres, this induced B_r would act against the ambient radial field, thereby generating local minima in the radial magnetic field intensity at the CMB. Interestingly, this scenario would generate a correlation between an inferred polar vortex and a polar minimum, but crucial to this scenario is the small-scale, unobserved nonaxisymmetric helical flow. For roughly uniform small-scale helical flow (cf. ref. 45), this process would tend to generate a relatively smooth polar minimum that would be predominantly axisymmetric in structure (e.g., case S2 in ref. 24), unlike the strongly nonaxisymmetric magnetic minima observed at the Earth's CMB (Fig. 1*A*). If both the α-effect and the ω-effect are strong inside TC, it is then possible to have a local $\alpha - \omega$ dynamo with a quasi-regularly flipping magnetic field inside the TC (e.g., see movie of case S2 in ref. 24; https://doi.org/10.6084/m9.figshare.4924223.v1).

In our second proposed scenario, large-scale nonaxisymmetric and/or time-varying polar upwellings would advect reversed magnetic flux patches outwards to the CMB (Fig. 4*B*), a process found to occur in a number of global numerical simulations (e.g., refs. 46 and 47). To generate strong polar magnetic minima, these polar plumes must be nonaxisymmetric or time-varying in nature, such that they are not in steady magnetostrophic balance. Downwelling plumes tend to generate magnetic maxima via focusing of magnetic fluxes. Thus, for this mechanism to consistently generate polar magnetic minima instead of polar magnetic maxima, the nonaxisymmetric upwelling plumes need to dominate the nonaxisymmetric downwelling plumes inside the TC. However, Sreenivasan and Jones (46) generally found a similar number of upwelling plumes and downwelling plumes inside TC (see their figure 9). If a similar number of upwelling and downwelling plumes is indeed typically the case, the nonaxisymmetric scenario would tend to generate large-scale nonaxisymmetric polar magnetic minima and maxima simultaneously.

Time-varying axisymmetric polar upwellings is an alternative, in which the axisymmetric upwelling can be much stronger than dictated by [**5**] during the strong acceleration phase of polar vortices. We noticed that in our lowest Ekman number 3D global simulations at $E = 10^{-6}$, there exist no significant polar magnetic minima except during a few snapshots (*SI Appendix*, Movie S1; also available at https://doi.org/10.6084/m9.figshare.7152665), which is in line with this scenario in which strong polar magnetic minima is a time-varying phenomenon.

Third, large-scale instability of the TC shear layer (Fig. 4*C*) could generate CMB magnetic field signals similar to those observed. For instance, present-day CMB B_r in the Earth's southern hemisphere features a strong azimuthal wavenumber one, $m = 1$, structure (Fig. 1*A*). Similarly, a $m = 1$ structure appears to exist along the TC in the recent geomagnetic secular variation inversion analysis of ref. 25. A number of mechanisms could generate such a $m = 1$ instability of the TC shear layer, including some form of magneto-rotational instability (48) or baroclinic instability of the TC (49).

The physics underlying these possibilities are rich, and their quantitative assessment under Earth's core conditions remains open to future research efforts. Further, if significant polar

magnetic structures are found in high-resolution magnetic field observation of other planetary bodies, such as Mercury (50), Jupiter (51), and Saturn (52, 53), our results suggest that physical processes beyond steady polar vortex flows are at play.

ACKNOWLEDGMENTS. We thank the editor and three reviewers for their constructive comments, which greatly improved this manuscript. J.M.A. gratefully acknowledges the support of the National Science Foundation Geophysics Program (Award EAR-1547269). The two higher Ekman number 3D dynamo simulations were carried out at Gesellschaft für wissenschaftliche Datenverarbeitung mbH, Göttingen (GWDG) and at Rechenzentrum Garching der Max-Planck-Gesellschaft (RZG). The lowest Ekman number case was carried out on the ALCF Mira supercomputer (DE-AC02-06CH11357) through the Innovative and Novel Computational Impact on Theory and Experiment (INCITE) program.

1. Hulot G, Finlay CC, Constable CG, Olsen CG, Mandea M (2010) The magnetic field of planet earth. *Space Sci Rev* 152:159–222.
2. Roberts PH, King EM (2013) On the genesis of the Earth's magnetism. *Rep Prog Phys* 76:096801.
3. Stevenson DJ (2003) Planetary magnetic fields. *Earth Planet Sci Lett* 208:1–11.
4. Schubert G, Soderlund KM (2011) Planetary magnetic fields: Observations and models. *Phys Earth Planet Inter* 187:92–108.
5. Olsen N, Finlay CC, Kotsiaros S, Tøffner-Clausen L (2016) A model of Earth's magnetic field derived from 2 years of Swarm satellite constellation data. *Earth, Planets, Space* 68:124.
6. Gubbins D, Bloxham J (1987) Morphology of the geomagnetic field and implications for the geodynamo. *Nature* 325:509–511.
7. Christensen U, Olson P, Glatzmaier GA (1998) A dynamo model interpretation of geomagnetic field structures. *Geophys Res Lett* 25:1565–1568.
8. Olson P, Christensen U, Glatzmaier GA (1999) Numerical modeling of the geodynamo: Mechanisms of field generation and equilibration. *J Geophys Res Solid Earth* 104:10383–10404.
9. Aurnou J, Andreadis S, Zhu L, Olson P (2003) Experiments on convection in Earth's core tangent cylinder. *Earth Planet Sci Lett* 212:119–134.
10. Sreenivasan B, Jones CA (2005) Structure and dynamics of the polar vortex in the Earth's core. *Geophys Res Lett* 32:L20301.
11. Christensen UR (2011) Geodynamo models: Tools for understanding properties of Earth's magnetic field. *Phys Earth Planet Inter* 187:157–169.
12. Olson P, Aurnou J (1999) A polar vortex in the Earth's core. *Nature* 402:170–173.
13. Hulot G, Eymin C, Langlais B, Mandea M, Olsen N (2002) Small-scale structure of the geodynamo inferred from Oersted and Magsat satellite data. *Nature* 416:620–623.
14. Amit H, Olson P (2004) Helical core flow from geomagnetic secular variation. *Phys Earth Planet Inter* 147:1–25.
15. Amit H, Olson P (2006) Time-average and time-dependent parts of core flow. *Phys Earth Planet Inter* 155:120–139.
16. Pozzo M, Davies C, Gubbins D, Alfè D (2012) Thermal and electrical conductivity of iron at Earth's core conditions. *Nature* 485:355–358.
17. Ohta K, Kuwayama Y, Hirose K, Shimizu K, Ohishi Y (2016) Experimental determination of the electrical resistivity of iron at Earth's core conditions. *Nature* 534:95–98.
18. Song X, Richards PG (1996) Seismological evidence for differential rotation of the Earth's inner core. *Nature* 382:221–224.
19. Aurnou JM, Brito D, Olson PL (1996) Mechanics of inner core super-rotation. *Geophys Res Lett* 23:3401–3404.
20. Glatzmaier GA, Roberts PH (1996) Rotation and magnetism of earth's inner core. *Science* 274:1887–1891.
21. Hollerbach R (1998) What can the observed rotation of the Earth's inner core reveal about the state of the outer core? *Geophys J Int* 135:564–572.
22. Tkalčić H, Young M, Bodin T, Ngo S, Sambridge M (2013) The shuffling rotation of the Earth's inner core revealed by earthquake doublets. *Nat Geosci* 6:497–502.
23. Livermore PW, Hollerbach R, Jackson A (2013) Electromagnetically driven westward drift and inner-core superrotation in Earth's core. *Proc Natl Acad Sci USA* 110:15914–15918.
24. Schaeffer N, Jault D,Nataf H-C, Fournier A (2017) Turbulent geodynamo simulations: A leap towards earth's core. *Geophys J Int* 211:1–29.
25. Livermore PW, Hollerbach R, Finlay CC (2017) An accelerating high-latitude jet in Earth's core. *Nat Geosci* 10:62–68.
26. Landeau M, Aubert J, Olson P (2017) The signature of inner-core nucleation on the geodynamo. *Earth Planet Sci Lett* 465:193–204.
27. Pedlosky J (1982) *Geophysical Fluid Dynamics* (Springer-Verlag, NY).
28. McWilliams JC (2006) *Fundamentals Geophys Fluid Dynamics* (Cambridge Univ Press, Cambridge, UK).
29. Vallis GK (2006) *Atmospheric and Oceanic Fluid Dynamics* (Cambridge Univ Press, Cambridge, UK).
30. Garaud P, Acevedo Arreguin L (2009) On the penetration of meridional circulation below the solar convection zone. II. Models with convection zone, the Taylor-Proudman constraint, and applications to other stars. *Astrophys J* 704:1–16.
31. Miesch MS, Hindman BW (2011) Gyroscopic pumping in the solar near-surface shear layer. *Astrophys J* 743:79.
32. Yadav RK, Gastine T, Christensen UR, Wolk SJ, Poppenhaeger K (2016) Approaching a realistic force balance in geodynamo simulations. *Proc Natl Acad Sci USA* 113:12065–12070.
33. Aubert J, Gastine T, Fournier A (2017) Spherical convective dynamos in the rapidly rotating asymptotic regime. *J Fluid Mech* 813:558–593.
34. Calkins MA, Julien K, Tobias SM (2017) Inertia-less convectively-driven dynamo models in the limit of low Rossby number and large Prandtl number. *Phys Earth Planet Inter* 266:54–59.
35. Roberts PH (1988) On topographic core-mantle coupling. *Geophys Astrophys Fluid Dyn* 44:181–187.
36. Taylor JB (1963) The magneto-hydrodynamics of a rotating fluid and the earth's dynamo problem. *Proc R Soc Lond Ser A* 274:274–283.
37. Hollerbach R, Ierley GR (1991) A modal α^2-dynamo in the limit of asymptotically small viscosity. *Geophys Astrophys Fluid Dyn* 56:133–158.
38. Livermore PW, Bailey LM, Hollerbach R (2016) A comparison of no-slip, stress-free and inviscid models of rapidly rotating fluid in a spherical shell. *Sci Rep* 6:22812.
39. Aubert J, Labrosse S, Poitou C (2009) Modelling the palaeo-evolution of the geodynamo. *Geophys J Int* 179:1414–1428.
40. Driscoll PE (2016) Simulating 2 Ga of geodynamo history. *Geophys Res Lett* 43:5680–5687.
41. Aubert J (2005) Steady zonal flows in spherical shell dynamos. *J Fluid Mech* 542:53–67.
42. Calkins MA, Julien K, Tobias SM, Aurnou JM (2015) A multiscale dynamo model driven by quasi-geostrophic convection. *J Fluid Mech* 780:143–166.
43. Ranjan A, Davidson PA (2014) Evolution of a turbulent cloud under rotation. *J Fluid Mech* 756:488–509.
44. Stellmach S, et al. (2014) Approaching the asymptotic regime of rapidly rotating convection: Boundary layers versus interior dynamics. *Phys Rev Lett* 113:254501.
45. Sreenivasan B, Gopinath V (2017) Confinement of rotating convection by a laterally varying magnetic field. *J Fluid Mech* 822:590–616.
46. Sreenivasan B, Jones CA (2006) Azimuthal winds, convection and dynamo action in the polar regions of planetary cores. *Geophys Astrophys Fluid Dyn* 100:319–339.
47. Aubert J, Aurnou J, Wicht J (2008) The magnetic structure of convection-driven numerical dynamos. *Geophys J Int* 172:945–956.
48. Seilmayer M, et al. (2014) Experimental evidence for nonaxisymmetric magnetorotational instability in a rotating liquid metal exposed to an azimuthal magnetic field. *Phys Rev Lett* 113:024505.
49. Gilman P, Dikpati M (2014) Baroclinic instability in the solar tachocline. *Astrophys J* 787:60.
50. Anderson BJ, et al. (2012) Low-degree structure in Mercury's planetary magnetic field. *J Geophys Res* 117:E00L12.
51. Moore KM, et al. (2018) A complex dynamo inferred from the hemispheric dichotomy of Jupiter's magnetic field. *Nature* 561:76–78.
52. Cao H, Russell CT, Wicht J, Christensen UR, Dougherty MK (2012) Saturn's high degree magnetic moments: Evidence for a unique planetary dynamo. *Icarus* 221:388–394.
53. Dougherty MK, et al. (2018) Saturn's magnetic field revealed by the Cassini Grand Finale. *Science* 362:eaat5434.

Supplementary Information Text

Numerical Implementation of Axisymmetric Magnetostrophic MHD Equations

Axisymmetric Decomposition of the Governing Equations under the Magnetostrophic Approximation. Following the work of Hollerbach (1), we have developed the numerical model described here to quantify how steady, axisymmetric meridional circulations, driven by gyroscopic pumping, can act to generate polar magnetic minima. For axisymmetric flows under the Boussinesq approximation ($\nabla\cdot\mathbf{U}=0$, $\partial/\partial\phi=0$, here $\mathbf{U}$ is the velocity and ϕ is the azimuthal angle), we adopt the axisymmetric decomposition for solenoidal fields:

$$\mathbf{B}(r,\theta)=\nabla\times(A\hat{\mathbf{e}_\phi})+B\hat{\mathbf{e}_\phi}, \tag{S1}$$

$$\mathbf{U}(r,\theta)=\nabla\times(\psi\hat{\mathbf{e}_\phi})+v\hat{\mathbf{e}_\phi}. \tag{S2}$$

In the axisymmetric decomposition, $(B_r,B_\theta)=\nabla\times(A\hat{\mathbf{e}_\phi})$ is the poloidal magnetic field while $B\hat{\mathbf{e}_\phi}$ is the toroidal magnetic field. The non-dimensional momentum equation under the zero inertia limit is

$$2\hat{z}\times\mathbf{U}+\nabla\Pi=(\nabla\times\mathbf{B})\times\mathbf{B}+\mathcal{A}_{\mathcal{TW}}T\vec{r}+E\nabla^2\mathbf{U}, \tag{S3}$$

and the non-dimensional electromagnetic induction equation is

$$\frac{\partial\mathbf{B}}{\partial t}=\nabla\times(\mathbf{U}\times\mathbf{B})+\nabla^2\mathbf{B}, \tag{S4}$$

where Π is the non-hydrostatic pressure, T is the temperature perturbation, $\hat{z}$ is the unit vector parallel to the spin-axis, and $\vec{r}$ is the radial vector from the center of the coordinate system. In this normalization, the length scale is the radius of the core R_C; the time scale is the magnetic diffusion time R_C^2/η in which η is the magnetic diffusivity; the magnetic field scale is $\sqrt{\mu_0\eta\rho_0\Omega}$ in which μ_0 is the magnetic permeability, ρ_0 is the fluid density, and Ω is the background rotation rate; the temperature scale is $\Omega\eta/\alpha g_0R_C$ in which α is the thermal expansivity and gravity is $\vec{g}=g_0\vec{r}$ such that g_0 is the gravitational acceleration at the model's core-mantle boundary (CMB); $\mathcal{A}_{\mathcal{TW}}$ is a coefficient used to vary the strength of the thermal forcing; and the Ekman number is defined as $E=\nu/\Omega R_C^2$ in which ν is the kinematic viscosity.

Due to the adoption of the magnetic diffusion time as the time scale, there is no need to define a magnetic Prandtl number, $Pm=\nu/\eta$, and the amplitude of the non-dimensional velocity here is simply the magnetic Reynolds number, $Rm=|\widetilde{\mathbf{u}}|R_C/\eta$, associated with the dimensional flow $\widetilde{\mathbf{u}}$. The amplitude of the non-dimensional magnetic field here is the square-root of the Elsasser number associated with the dimensional magnetic field $\widetilde{\mathbf{B}}$, where the Elsasser number Λ is defined as $\Lambda=|\widetilde{\mathbf{B}}|^2/\mu_0\eta\rho_0\Omega$.

There are three control parameters in our numerical experiments: 1) the Ekman number E; 2) the amplitude of the thermal forcing $\mathcal{A}_{\mathcal{TW}}$; and 3) the amplitude and geometry of the imposed poloidal magnetic field. We quantify the amplitude of the imposed magnetic field with the Elsasser number Λ_{imp}. The geometry of the imposed magnetic field are varied via different combinations of associated Legendre polynomials. In our model, current-free poloidal magnetic field with varying amplitudes and geometries have been imposed through appropriate magnetic boundary conditions. See subsection **Magnetic Boundary Conditions** for details.

The above non-dimensional momentum equation under the axisymmetric decomposition becomes

$$2\frac{\partial}{\partial z}\psi+ED^2v=-N(B,A), \tag{S5}$$

$$2\frac{\partial}{\partial z}v-ED^4\psi=M(B,B)+M(D^2A,A)+\frac{\partial T(r,\theta)}{\partial\theta}, \tag{S6}$$

in which

$$D^2=\nabla^2-\frac{1}{r^2\sin^2\theta}, \tag{S7}$$

$$N(X,Y)=\hat{\mathbf{e}_\phi}\cdot[\nabla\times(X\hat{\mathbf{e}_\phi})\times\nabla\times(Y\hat{\mathbf{e}_\phi})], \tag{S8}$$

$$M(X,Y)=\hat{\mathbf{e}_\phi}\cdot\nabla\times[X\hat{\mathbf{e}_\phi}\times\nabla\times(Y\hat{\mathbf{e}_\phi})]. \tag{S9}$$

The flows in our models are driven by the latitudinal gradient of the axisymmetric temperature field, $\partial T(r,\theta)/\partial\theta$, the rightmost term in Eq. [S6]. This temperature pattern, $T(r,\theta)$, is taken from a three-dimensional dynamo calculation described below in section **Thermal Forcing**. There is no $1/r$ factor in front of the $\partial T/\partial\theta$ term due to the use of the radial vector $\vec{r}$ instead of the unit vector in the radial direction $\hat{r}$ for the buoyancy term.

Under the axisymmetric decomposition, the non-dimensional induction equation becomes

$$\frac{\partial A}{\partial t}+\frac{1}{s}\nabla\times(\psi\hat{\mathbf{e}_\phi})\cdot\nabla(sA)=D^2A, \tag{S10}$$

$$\frac{\partial B}{\partial t}+s\nabla\cdot\left[\frac{B}{s}\nabla\times(\psi\hat{\mathbf{e}_\phi})\right]=s(\nabla\times A\hat{\mathbf{e}_\phi})\cdot\nabla\omega+D^2B, \tag{S11}$$

in which $s=r\sin\theta$ and ω is the angular velocity $\omega=v/s$. In this axisymmetric system, we do not consider any dynamo α-effect.

Spectral Equation for Numerical Calculations. Given that $D^2 = \left(\nabla^2 - 1/s^2\right)$ is the diffusion operator in the MHD equations under axisymmetry in the spherical coordinates, the natural functional bases to express ψ, v, A, and B are order-1 associated Legendre polynomials $P_n^1(\cos\theta)$, for which

$$\left(\nabla^2 - \frac{1}{s^2}\right) P_n^1(\cos\theta) = -\frac{n(n+1)}{r^2} P_n^1(\cos\theta). \quad [S12]$$

It should be emphasized here that order-1 associated Legendre polynomials are only functions of θ (e.g. Chapters 8 and 12 in (2)).

Projecting ψ, v, A, and B onto P_n^1 yields

$$\psi = \sum_{n=1}^{N_{max}} \psi_n(r) P_n^1(\mu), \quad [S13]$$

$$v = \sum_{n=1}^{N_{max}} v_n(r) P_n^1(\mu), \quad [S14]$$

$$A = \sum_{n=1}^{N_{max}} a_n(r) P_n^1(\mu), \quad [S15]$$

$$B = \sum_{n=1}^{N_{max}} b_n(r) P_n^1(\mu), \quad [S16]$$

where $\mu = \cos\theta$.

For the diffusion operators, it can be shown that

$$D_n^2 = \left[\frac{d^2}{dr^2} + \frac{2}{r}\frac{d}{dr} - \frac{n(n+1)}{r^2}\right], \quad [S17]$$

$$D_n^4 = \left[\frac{d^4}{dr^4} + \frac{4}{r}\frac{d^3}{dr^3} - \frac{2n(n+1)}{r^2}\frac{d^2}{dr^2} - \frac{4n(n+1)}{r^3}\frac{d}{dr} + \frac{n^2(n+1)^2 - 2n(n+1)}{r^4}\right]. \quad [S18]$$

For the $\partial/\partial z$ operators,

$$\frac{\partial}{\partial z} = s\theta\frac{\partial}{\partial r} - \frac{\sin\theta}{r}\frac{\partial}{\partial\theta}, \quad [S19]$$

$$\frac{\partial}{\partial z} v = \sum_{n=1}^{N_{max}} \left[\frac{dv_n}{dr}\mu P_n^1(\mu) + \frac{v_n}{r}\left(1-\mu^2\right)\frac{dP_n^1}{d\mu}\right]. \quad [S20]$$

Making use of the following two recurrence properties,

$$\mu P_n^1 = \frac{(n+1)P_{n-1}^1 + nP_{n+1}^1}{2n+1}, \quad [S21]$$

$$\left(1-\mu^2\right)\frac{dP_n^1}{d\mu} = \frac{(n+1)^2 P_{n-1}^1 - n^2 P_{n+1}^1}{2n+1}, \quad [S22]$$

and adopting full normalization to the associated Legendre polynomials, one can show that the left-hand-sides of the momentum equations, [S5] and [S6], can be recast as

$$\sqrt{\frac{(n+1)(n-1)}{\left(n+\frac{1}{2}\right)\left(n-\frac{1}{2}\right)}}\left(\frac{d\psi_{n-1}}{dr} - \frac{n-1}{r}\psi_{n-1}\right) + \sqrt{\frac{(n+2)n}{\left(n+\frac{3}{2}\right)\left(n+\frac{1}{2}\right)}}\left(\frac{d\psi_{n+1}}{dr} + \frac{n+2}{r}\psi_{n+1}\right) + ED_n^2 v_n, \quad [S23]$$

$$\sqrt{\frac{(n+1)(n-1)}{\left(n+\frac{1}{2}\right)\left(n-\frac{1}{2}\right)}}\left(\frac{dv_{n-1}}{dr} - \frac{n-1}{r}v_{n-1}\right) + \sqrt{\frac{(n+2)n}{\left(n+\frac{3}{2}\right)\left(n+\frac{1}{2}\right)}}\left(\frac{dv_{n+1}}{dr} + \frac{n+2}{r}v_{n+1}\right) - ED_n^4\psi_n.$$

Nonlinear Terms. The nonlinear terms associated with operators M & N are evaluated in real space first, then project onto P_n^1 (3).

Mechanical Boundary Conditions. The no-slip mechanical boundary condition reads

$$\psi_n = \frac{d}{dr}\psi_n = 0, \tag{S24}$$

$$v_n = 0, \tag{S25}$$

while the free-slip mechanical boundary condition reads

$$\psi_n = \frac{d^2}{dr^2}\psi_n = 0, \tag{S26}$$

$$\frac{dv_n}{dr} - \frac{v_n}{r} = 0. \tag{S27}$$

Magnetic Boundary Conditions. The vacuum outer boundary condition for magnetic field is

$$b_n(r_o) = 0, \tag{S28}$$

$$\frac{da_n}{dr} + \frac{n+1}{r}a_n = B_0^n, \tag{S29}$$

here B_0^n is the projection of the imposed magnetic field onto P_n^1. For example, to impose a uniform magnetic field of amplitude B_{imp} in the z direction, one would set $B_0^1 = \sqrt{3}B_{imp}$ and $B_0^{n>1} = 0$ (see Fig S1 panel (c) for an associated example). The $\sqrt{3}$ factor comes from the normalization of the associated Legendre polynomials. To impose a magnetic field with more complex geometry, e.g. $B_z + cB_s$, one could set $B_0^1 = \sqrt{3}B_{imp}$, $B_0^3 = \sqrt{3}cB_{imp}$, and $B_0^{n>3} = 0$ (see Fig S1 panel (d) for an associated example). The finite conducting steady-state inner boundary condition for magnetic field is

$$\frac{db_n}{dr} - \frac{n}{r}b_n = 0, \tag{S30}$$

$$\frac{da_n}{dr} - \frac{n}{r}a_n = 0. \tag{S31}$$

Thermal Forcing

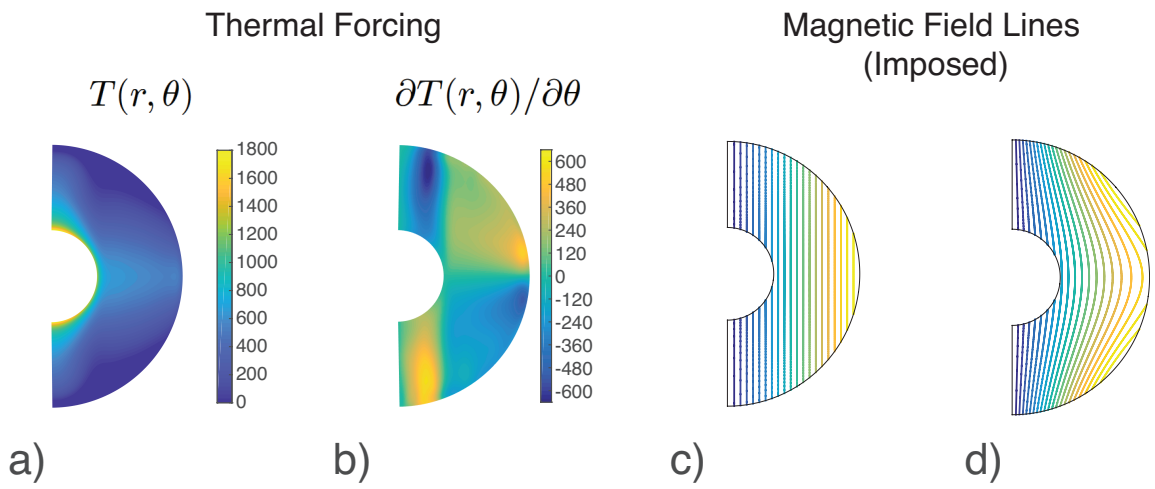

Fig. S1. Thermal forcing pattern a) $T(r,\theta)$ and b) $\partial T(r,\theta)/\partial\theta$, shown with amplitude $\mathcal{A}_{\mathcal{TW}} = 600$. The temperature scale is $\Omega\eta/\alpha g_0 R_C$, in which R_C is the radius of the core, Ω is the background rotation rate, α is the thermal expansivity and g_0 is the gravitational acceleration at the CMB. This pattern is the result of a single three-dimensional self-consistent dynamo run carried out using the community dynamo code MagIC (https://magic-sph.github.io/). c) Axial imposed poloidal magnetic field, B_z. d) 'Mixed' imposed poloidal magnetic field, $B_z + cB_s$, where $c = 30\%$.

The pattern of the thermal wind forcing $\partial T(r,\theta)/\partial\theta$ shown in Figure S1b drives the flow in our axisymmetric, magnetostrophic models through the rightmost term in Eq. [S6]. This pattern is taken from a single three-dimensional global geodynamo simulation carried out with the following parameter values $(E, Ra, Pr, Pm) = (10^{-4}, 5\times10^7, 1, 2)$. The solution is an axial dipole dominant dynamo solution. The thermal wind forcing pattern $\partial T(r,\theta)/\partial\theta$ comes from the time and azimuthal average of the solution over 2 magnetic diffusion times. The mechanical boundary conditions are non-slip and the spherical shell geometry is Earth-like, with a radius ratio $r_{ICB}/r_{CMB} = 0.35$. Fixed homogeneous heat flux conditions are adopted at the top and bottom boundaries with zero heat sources in the outer core. The Ekman number is defined here as

$$E = \frac{\nu}{\Omega D^2}, \tag{S32}$$

the Prandtl number is defined as

$$Pr = \frac{\nu}{\kappa}, \quad [S33]$$

the Magnetic Prandtl number is defined as

$$Pm = \frac{\nu}{\eta}, \quad [S34]$$

and the Rayleigh number is defined as

$$Ra = \frac{\alpha g_0 q_0 D^4}{k\kappa\nu}, \quad [S35]$$

where ν is the kinematic viscosity, Ω is the rotation rate, $D = r_o - r_i$ is the shell thickness, r_o and r_i are the outer and inner boundary radii respectively, α is the thermal expansivity, g_0 is the gravitational acceleration on the core mantle boundary, k is the thermal conductivity, κ is the thermal diffusivity, and η is the magnetic diffusivity, and q_0 is the outer boundary heat flow.

The open-source numerical dynamo code MagIC has been used for the three-dimensional global geodynamo simulation (https://magic-sph.github.io/). Here, we used MagIC to solve the following non-dimensional governing equations under the Boussinesq approximation.

$$\nabla \cdot \boldsymbol{u} = 0, \ \nabla \cdot \boldsymbol{B} = 0, \quad [S36]$$

$$E(\frac{\partial \boldsymbol{u}}{\partial t} + \boldsymbol{u} \cdot \nabla \boldsymbol{u}) + 2\boldsymbol{e}_z \times \boldsymbol{u} + \nabla \Pi = E\nabla^2 \boldsymbol{u} + \frac{RaE}{Pr}\frac{\boldsymbol{r}}{r_o}T + \frac{1}{Pm}(\nabla \times \boldsymbol{B}) \times \boldsymbol{B}, \quad [S37]$$

$$\frac{\partial \boldsymbol{B}}{\partial t} = \nabla \times (\boldsymbol{u} \times \boldsymbol{B}) + \frac{1}{Pm}\nabla^2 \boldsymbol{B}, \quad [S38]$$

$$\frac{\partial T}{\partial t} + \boldsymbol{u} \cdot \nabla T = \frac{1}{Pr}\nabla^2 T, \quad [S39]$$

where $\boldsymbol{u}$ is the velocity, $\boldsymbol{B}$ is the magnetic field, Π is the non-hydrostatic effective pressure, T is the temperature perturbation.

We have fixed the pattern of the thermal forcing in all our numerical magnetostrophic runs. The underlying physical picture for this assumption is that it is the expected convective flows that determines the main thermal structure of the outer core: warm TC (relatively inefficient convective cooling inside TC compared to that at mid-latitude), cold mid-latitude (very efficient convective cooling of mid-latitude via large-scale columnar convection), warm equatorial region (inefficient convective cooling since convective motion is preferred in the direction perpendicular to the equatorial plane). Such thermal structure would give rise to the thermal forcing pattern investigated here: negative $\partial T(r,\theta)/\partial\theta$ in the northern TC, positive $\partial T(r,\theta)/\partial\theta$ outside TC in the northern hemisphere, while the southern hemisphere is simply antisymmetric to that in the north (see Fig. S1). We do expect such general pattern, not the amplitude, to remain independent of the Ekman, Rayleigh number as long as the resulted magnetic field are dipolar. We further examined 3D global numerical dynamo models with Ekman number varying from 10^{-4} to 10^{-6}, and found the same bulk temperature features: warm TC, cold mid-latitude, and warm equatorial regions.

The amplitude of the thermal forcing is set by the value of $\mathcal{A}_{\mathcal{TW}}$. $\mathcal{A}_{\mathcal{TW}}$ of 300 would give rise to a total zonal velocity shear within the TC, defined as $Rm(u_\phi, TC)_{max} - Rm(u_\phi, TC)_{min}$, around 100, while $\mathcal{A}_{\mathcal{TW}}$ of 6000 would give rise to a total zonal velocity shear within the TC around 2000.

Gyroscopic Pumping Describes a Balanced State

We emphasize that steady meridional flows, regardless being of thermal plume origin or of Lorentz force origin, is in the same magnetostrophic balance as investigated in our study. The steady-state force/vorticity balance equations (equations [7], [S5], [S6]) describe the equilibrium state of the system, without specifying whether it is the meridional circulation (thermal plume) that drives the zonal flow (polar vortex) or it is the zonal flow that drives the meridional circulation. In steady state, the system is in the same force/vorticity balance. Sreenivasan and Jones (4, 5) are important works on tangent cylinder magnetohydrodynamics. We would like to point out that equation [7] in Sreenivasan and Jones (4) is the same as our equation [S5].

Within the framework of meridional circulation driven polar magnetic minima, the defining factor on the resulted polar magnetic minima is not the upwelling flow u_z, but the cylindrical radial flow u_s. Although u_z and u_s are related through mass conservation, strong upwelling flow does not necessarily result in consistent large-scale cylindrical radial out flow. As a counter example, thin downwelling channels could fulfill the requirement of mass conservation. For steady large-scale cylindrical radial flow u_s within the Earth's outer core, the Coriolis force associated with it is most likely balanced by the Lorentz force, as shown by equations [S5] (in which the first term on the LHS is u_s, while the term on the RHS is the Lorentz force) and Fig. S5ab. This is also true under non-axisymmetry, since pressure gradient cannot balance z-varying flows and u_s associated with upwelling must be z-varying to conserve mass. As shown by our scaling equation [5] and dynamical magnetostrophic models, steady meridional circulation features magnetic Reynolds number on the order of $\sqrt{\Lambda(B_{r,\theta})}\sqrt{\Lambda(B_\phi)}$. Under the condition of the Earth's outer core, there is no obvious candidate to balance meridional circulation much stronger than this. Thus, this suggests that large-scale meridional circulation with Rm much greater than unity, if exist within Earth's outer core, likely is strongly time varying.

Global 3D Numerical Dynamo Simulations

The snapshot magnetic fields shown in Figure 4 are from a subset of global 3D numerical dynamo simulations, the force-balance of which have been reported in (6). Please see the **Method** section in (6) for the exact equations and normalization.

In particular, we selected various E cases from (6) in which $Rm(u_\phi, TC) \sim 200$. In all three cases, the boundary conditions are fixed temperature, no-slip, and potential magnetic fields. The non-dimensional control parameters in these three selected cases are $(E, Ra, Pr, Pm) = (10^{-4}, 7 \times 10^6, 1, 1)$, $(E, Ra, Pr, Pm) = (10^{-5}, 10^8, 1, 1)$, $(E, Ra, Pr, Pm) = (10^{-6}, 3 \times 10^9, 1, 0.5)$ respectively. The supercriticality are very similar for all three Ekman number cases: it is $\sim$10 for the $E = 10^{-4}$ run, $\sim$10 for the $E = 10^{-5}$ run, and $\sim$ 15 for the $E = 10^{-6}$ run.

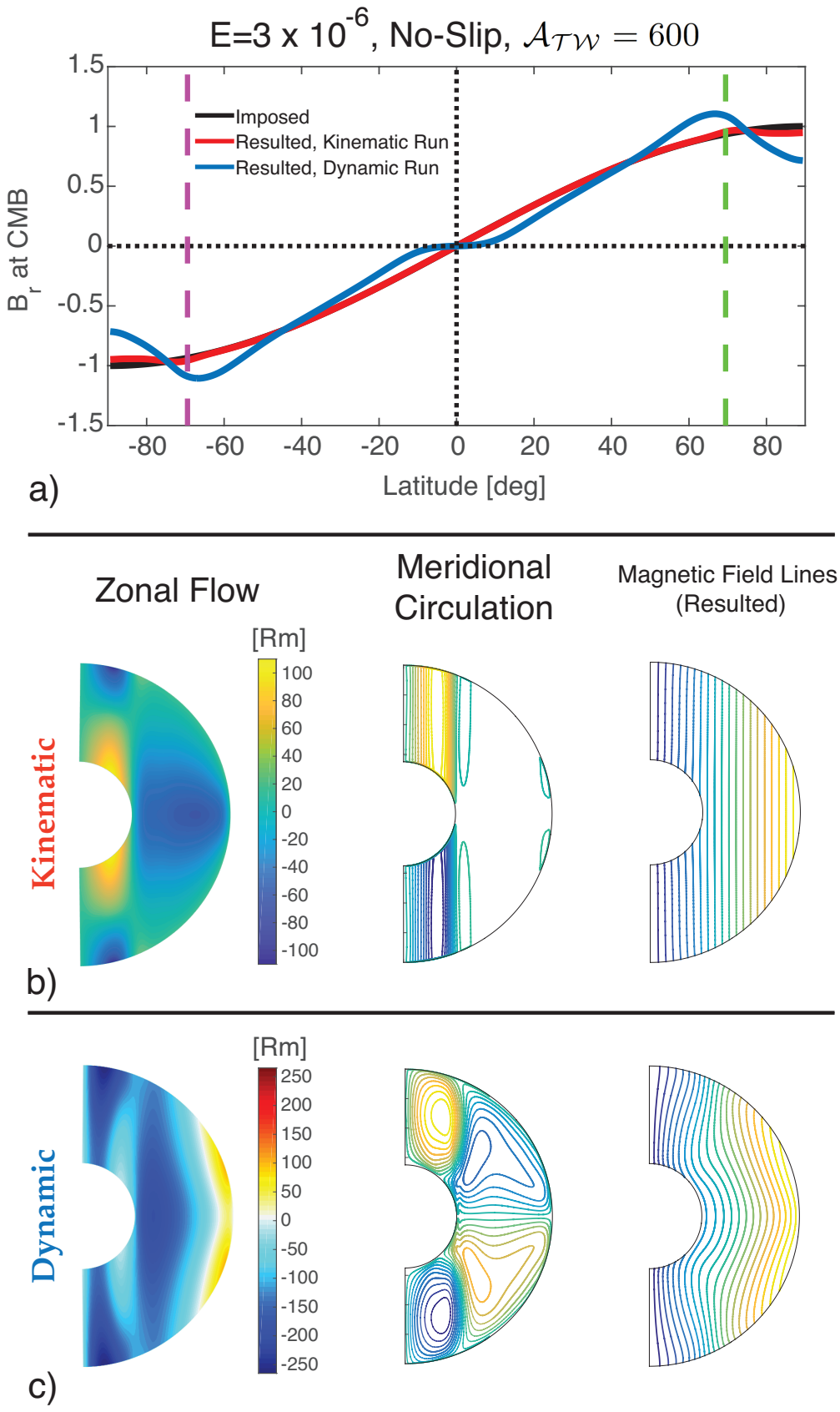

Fig. S2. Panel a) shows radial magnetic field patterns on the outer boundary (CMB) of no-slip models with $E = 3 \times 10^{-6}$, $\mathcal{A}_{\mathcal{TW}} = 600$, and an axial $\Lambda_{imp} = 1$ imposed magnetic field (black line). The red (blue) line shows the radial field in the kinematic (dynamic) calculation. Panel b) and c) show the resulting patterns of zonal velocity (left), meridional circulation (center) and meridional magnetic fields (right), respectively, in the kinematic and dynamic cases.

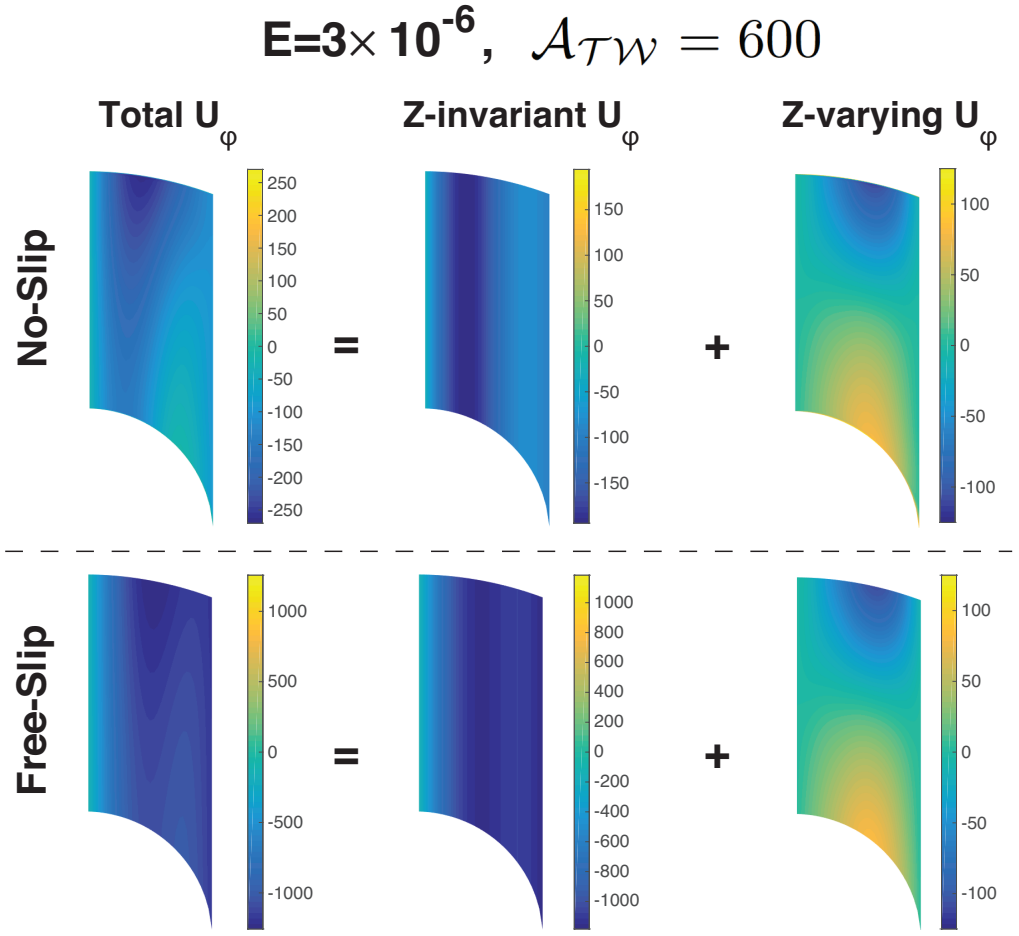

Fig. S3. Zonal flows inside the tangent cylinder in two dynamic runs under the same forcing and parameters with no-slip (upper panels) and free-slip (lower panels) mechanical boundary conditions. The left most panels show the total zonal flows, the middle panels show the z-invariant zonal flows, and the right most panels show the z-varing zonal flows. The Ekman is 3×10^{-6}, the amplitude of the thermal wind forcing $\mathcal{A}_{\mathcal{TW}} = 600$, and the imposed magnetic field is a uniform B_z field with amplitude $\Lambda(B_z) = 1$. It can be seen that under the same thermal wind forcing, similar z-varing zonal flows were generated, but very different z-invariant zonal flows results from the violation of Taylor's constraint under different mechanical boundary conditions. In both cases, the amplitude of the z-invariant zonal flows exceeds that of the z-varing zonal flows.

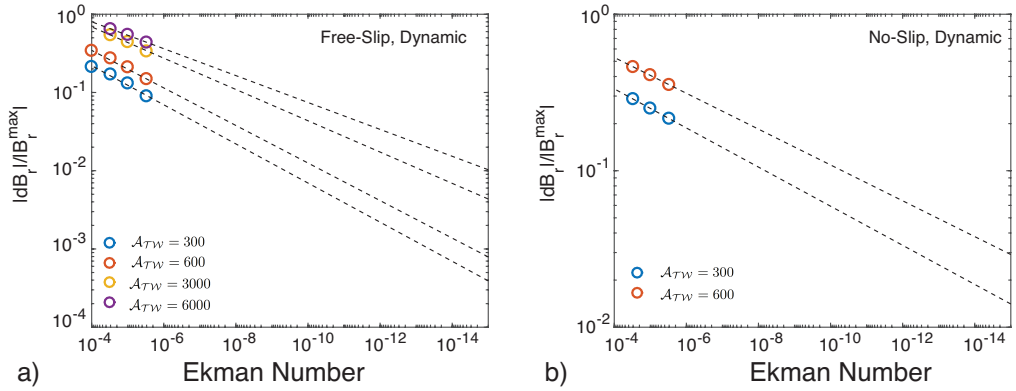

Fig. S4. Scaling of polar magnetic minima $|dB_r|/|B_r^{max}|$ in dynamic runs as a function of Ekman number at different $\mathcal{A}_{\mathcal{TW}}$. It can be seen that the resulted $|dB_r|/|B_r^{max}|$ at different $\mathcal{A}_{\mathcal{TW}}$ features similar scalings with the Ekman number in our dynamic surveys. However, the amplitude of $|dB_r|/|B_r^{max}|$ does not scale linearly with $\mathcal{A}_{\mathcal{TW}}$. For example, $|dB_r|/|B_r^{max}|$ only increases by a factor of 3 to 5 when we increase $\mathcal{A}_{\mathcal{TW}}$ by a factor of 10 (from 300 to 3000). We do expect the slope of $|dB_r|/|B_r^{max}|$ to be a function of $\mathcal{A}_{\mathcal{TW}}$, since the slope is controlled by the Lorentz force which would scale with $\mathcal{A}_{\mathcal{TW}}$. The derived scaling of polar magnetic minima are $2.2E^{1/4}$, $3.15E^{0.24}$, $4.74E^{1/5}$, $3.9E^{0.17}$ for $\mathcal{A}_{\mathcal{TW}} = (300, 600, 3000, 6000)$ free-slip cases, and $1.06E^{1/8}$, $1.52E^{0.115}$ for $\mathcal{A}_{\mathcal{TW}} = (300, 600)$ no-slip cases.

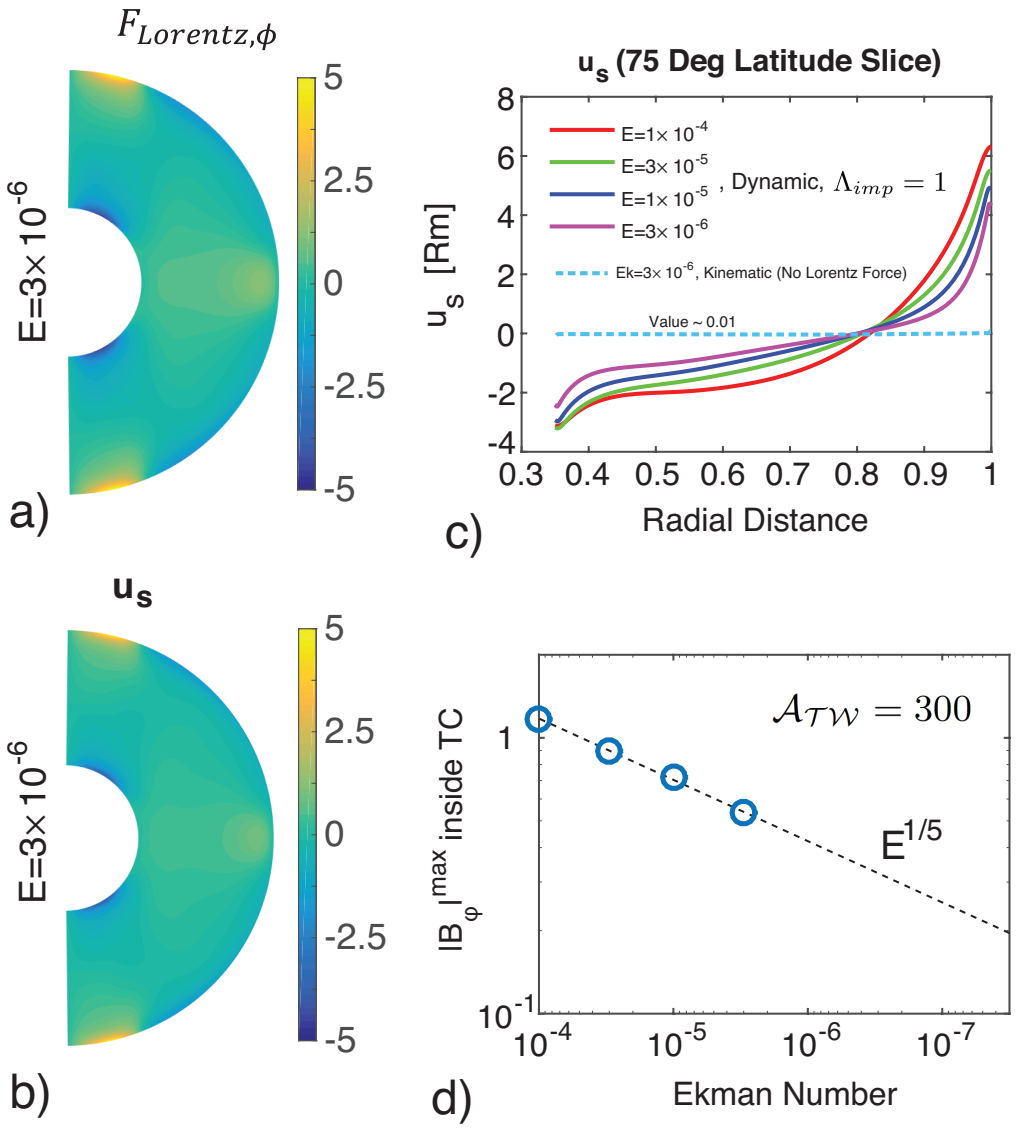

Fig. S5. Zonal Lorentz force, meridional circulation, and zonal (toroidal) magnetic field from our numerical surveys. Panel a & b shows that the zonal Lorentz force is locally balanced by the Coriolis force; this balance drives u_s while mass conservation drives u_z which completes the meridional circulation. Panel c shows a slice of meridional circulation u_s inside the tangent cylinder at 75 degrees latitude from a suite of dynamic calculations, and that from the corresponding kinematic calculation at $E = 3 \times 10^{-6}$. Panel d shows that the peak amplitude of B_ϕ inside the tangent cylinder follows a $E^{1/5}$ scaling in the dynamic calculations. B_ϕ results from the ω-effect, thus serves as a measure of the mis-alignment between the zonal flow and the poloidal magnetic field.

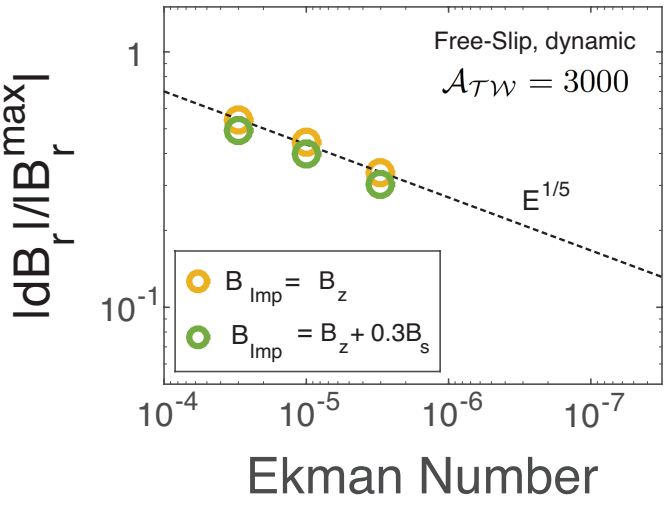

Fig. S6. Scaling of polar magnetic minima $|dB_r|/|B_r^{max}|$ in dynamic runs as a function of Ekman number with different geometries of imposed magnetic field (see Fig. S1). In these cases, $\mathcal{A}_{\mathcal{TW}} = 3000$, $\Lambda_{imp} = 1$, and free-slip mechanical boundary conditions have been adopted. It can be seen that the geometry of the imposed axisymmetric magnetic field does not fundamentally alter the amplitude and scaling of the resulted polar magnetic minima (cf. 7). Thus, our results are robust to variations in axisymmetric field geometry.

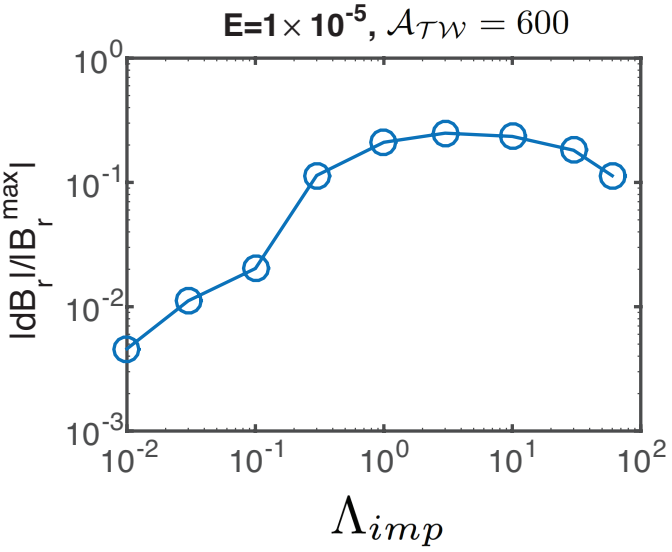

Fig. S7. Relative amplitude of polar magnetic mimina, $|dB_r|/|B_r^{max}|$, as a function of the Elsasser number of the imposed magnetic field in the dynamic calculations, Λ_{imp}. The value of $|dB_r|/|B_r^{max}|$ reaches its maximum in the range $\Lambda_{imp} \simeq 1$ - 10. The relative amplitude of the polar magnetic minima drops rapidly for both $\Lambda_{imp} \lesssim 1$ and $\Lambda_{imp} \gtrsim 10$.

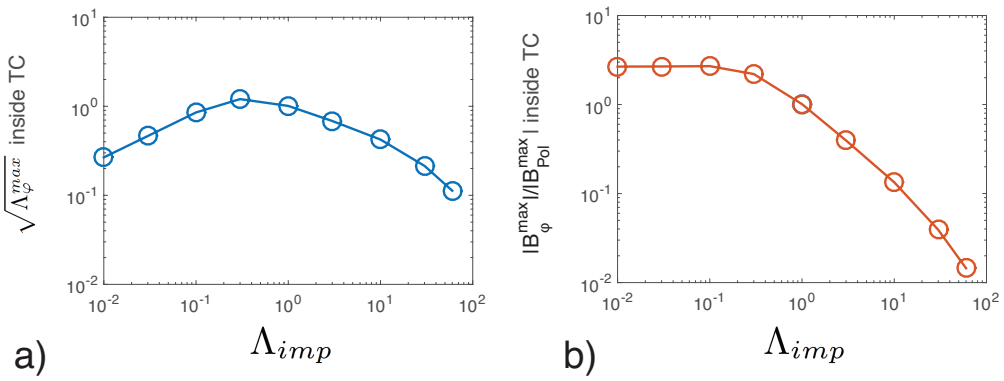

Fig. S8. Amplitude of maximum $|B_\phi|$ inside the TC as a function of the Elsasser number of the imposed magnetic field in our dynamic calculations. Panel a shows the amplitude of maximum TC $|B_\phi|$ in unit of the square root of the Elsasser number $\sqrt{\Lambda_\phi^{max}}$, while panel b shows the ratio of maximum TC $|B_\phi|$ to the amplitude of the imposed magnetic field $\sqrt{\Lambda_\phi^{max}/\Lambda_{imp}}$. These results show that i) $\sqrt{\Lambda_\phi^{max}}$ never exceeds 2 and that ii) $\sqrt{\Lambda_\phi^{max}/\Lambda_{imp}}$ decreases rapidly as Λ_{imp} increases above unity in our dynamic calculations. This further illustrates the strong feedback from the Lorentz force which better aligns the zonal flow with the poloidal magnetic field as $\Lambda(B_{r,\theta})$ increases beyond 1.

Movie S1. Time series of axisymmetric CMB B_r from a 3D numerical dynamo simulation. The non-dimensional control parameters are $(E, Ra, Pr, Pm) = (10^{-6}, 3 \times 10^9, 1, 0.5)$, and the resulted $Rm(u_\phi, TC) \sim 200$. The vertical dashed lines in the movie denote the boundary of tangent cylinder. It can be seen that there exist no significant polar magnetic minima in this low Ekman number 3D run except during a few snapshots.

References

1. Hollerbach R (1998) What can the observed rotation of the Earth's inner core reveal about the state of the outer core? *Geophysical Journal International* 135:564–572.
2. Abramowitz M, Stegun IA (1970) *Handbook of mathematical functions : with formulas, graphs, and mathematical tables.*
3. Glatzmaier GA (2013) *Introduction to Modelling Convection in Planets and Stars.* (Princeton University Press, Princeton, NJ).
4. Sreenivasan B, Jones CA (2005) Structure and dynamics of the polar vortex in the Earth's core. *Geophysical Research Letters* 32:L20301.
5. Sreenivasan B, Jones CA (2006) Azimuthal winds, convection and dynamo action in the polar regions of planetary cores. *Geophysical and Astrophysical Fluid Dynamics* 100:319–339.
6. Yadav RK, Gastine T, Christensen UR, Wolk SJ, Poppenhaeger K (2016) Approaching a realistic force balance in geodynamo simulations. *Proceedings of the National Academy of Science* 113:12065–12070.
7. Labbé F, Jault D, Gillet N (2015) On magnetostrophic inertia-less waves in quasi-geostrophic models of planetary cores. *Geophysical and Astrophysical Fluid Dynamics* 109:587–610.